Sharp-Crested Breaking Surface Waves Observed from a Ship-Based Stereo Video System

MICHAEL S. SCHWENDEMAN AND JIM THOMSON

Applied Physics Laboratory, University of Washington, Seattle, Washington

(Manuscript received 9 August 2016, in final form 24 January 2017)

ABSTRACT

A new ship-based stereo video system is used to observe breaking ocean waves (i.e., whitecaps) as three-dimensional surfaces evolving in time. First, the stereo video measurements of all waves (breaking and non-breaking) are shown to compare well with statistical parameters from traditional buoy measurements. Next, the breaking waves are detected based on the presence of whitecap foam, and the geometry of these waves is investigated. The stereo measurements show that the whitecaps are characterized by local extremes of surface slope, though the larger-scale, crest-to-trough steepness of these waves is unremarkable. Examination of 103 breaking wave profiles further demonstrates the pronounced increase in the local wave steepness near the breaking crest, as estimated using a Hilbert transform. These crests are found to closely resemble the sharp corner of the theoretical Stokes limiting wave. Results suggest that nonlinear wave group dynamics are a key mechanism for breaking, as the phase speed of the breaking waves is slower than predicted by the linear dispersion relation. The highly localized and transient steepness, along with the deviation from linear phase speed, explains the inability of conventional wave buoys to observe the detailed geometry of breaking waves.

1. Introduction

The breaking of surface waves in deep water has been an active topic of research for decades because of its importance for safety at sea, wave forecasting, and air–sea interactions (Melville 1996). Progress has been slow, as the physics of breaking are complex, and the necessary measurements challenging. As discussed in Babanin (2011), two questions in particular remain unresolved: what causes a wave to break (breaking onset), and how much wave energy is lost during breaking (breaking dissipation)? Advances have been made primarily through numerical and laboratory simulations, as measurements of oceanic breakers, or "whitecaps," are particularly difficult (Perlin et al. 2013). In this paper, observations of whitecaps are presented from a ship-based stereo video system. The focus is on the geometry of the breaking waves, especially their steepness, which is thought to be a critical factor for both onset and dissipation.

In deep water, the geometry of a linear monochromatic wave is fully determined by just two parameters, the wave height H and wavelength L, and thus the steepness may be described as simply the ratio H/L. In a real wave environment, however, the waves are neither monochromatic nor linear, which complicates the description of the wave geometry. Still, the steepness is often discussed using the familiar H/L ratio, or sometimes ak, where $a = H/2$ is the wave amplitude and $k = 2\pi/L$ is the radian wavenumber. Stokes (1880) was the first to derive a limiting condition for the geometry of a propagating surface wave, which is a sharp crest forming a 120° corner. Mathematically, the peak of the limiting crest forms a singularity where the underlying fluid velocity exactly matches the phase speed of the crest. It has been shown that such a crest is formed for a monochromatic nonlinear wave with steepness $H/L \approx 1/7$ or $ak \approx 0.443$ (e.g., Williams 1981). Whereas a monochromatic plane wave has its maximum slope at the mean water line, the limiting Stokes wave is steepest at the crest.

The Stokes limit was thus the first supposed breaking criterion, the assumption being that waves would grow

Denotes content that is immediately available upon publication as open access.

Supplemental information related to this paper is available at the Journals Online website: http://dx.doi.org/10.1175/JPO-D-16-0187.s1.

Corresponding author e-mail: Michael S. Schwendeman, mss28@u.washington.edu

DOI: 10.1175/JPO-D-16-0187.1

until this limiting geometry, at which point they would break. However, measurements from laboratory waves (Rapp and Melville 1990) and field experiments (Holthuijsen and Herbers 1986; Weissman et al. 1984) have suggested that waves break well below the Stokes steepness. In a field study using buoy estimates of steepness and human observers to detect breaking, Holthuijsen and Herbers (1986) found that whitecaps could not be distinguished from nonbreaking waves by their bulk H/L steepness alone (although the breaking waves were found to be slightly steeper on average than the nonbreaking waves). On the other hand, some laboratory experiments, including those of Brown and Jensen (2001) and Tian et al. (2010), have shown waves breaking near the Stokes limiting steepness. In particular, Babanin et al. (2007) made a renewed case for the applicability of the Stokes limit.

One complicating factor in comparing these previous studies is conflicting definitions of the wave steepness. For example, a single characteristic steepness is often calculated for many waves based on a spectral average (as in Banner et al. 2000) or experimental input parameters (Rapp and Melville 1990). Alternatively, studies like Holthuijsen and Herbers (1986) and Babanin et al. (2007) estimate the bulk steepness of individual waves, using a zero-crossing methodology to define the wave extent. Others have measured instead the local surface slope (see Brown and Jensen 2001; Tian et al. 2012). One study that examined both the wave-by-wave steepness and local slope around wave breaking is Chalikov and Babanin (2012). In a series of numerical experiments, they studied the onset of breaking using the fully nonlinear Chalikov–Sheinin model (Chalikov 2005), initialized from a JONSWAP spectrum with random phase components. The data showed that the bulk steepness of the breaking waves was much below that of the Stokes limiting wave and did not significantly increase prior to breaking. Conversely, the development of large surface slopes near the wave crest was the most consistent indication of imminent breaking. These sharp crest features were highly localized and often developed within fractions of a wave period from the breaking point.

Wave steepness has also been shown to be an important factor in the dissipation of wave energy during breaking. For example, Rapp and Melville (1990) showed that the relative energy loss was strongly dependent on the average wave steepness, with some scatter due to the packet bandwidth and central wavenumber. Similar results have since been shown in Banner and Pierson (2007), Drazen et al. (2008), and Tian et al. (2010). Again, differences in calculating the wave steepness, as well as the energy flux, make comparing across the studies somewhat difficult. However, the general agreement is that steeper waves lose a larger percentage of their energy flux during breaking.

The idea of using stereo imagery to measure ocean waves has a long history (see, e.g., Holthuijsen 1983), but only recently has it become realizable for most researchers. This is due to the rapid growth in computing power and camera technology as well as the increasing availability of sophisticated computer vision algorithms. In stereo video, pixels are matched between images from two or more cameras overlooking the same patch of the sea surface. Through triangulation, the distance to the water surface is estimated at each pixel, which produces a three-dimensional reconstruction of the surface. The ability to resolve the spatial wave geometry is a distinct advantage over point-based in situ wave measurements, such as buoys and wave staffs.

Still, measuring waves with stereo imagery has its own difficulties. Jähne et al. (1994) provides a critical review of the theoretical limitations, including resolution, occlusion, and specular reflection. Benetazzo (2006) gives a good overview of early efforts at stereo video and provides quantitative estimates of the errors involved. Benetazzo (2006), Wanek and Wu (2006), and de Vries et al. (2011) showed that measurements of waves with stereo video compared well with more traditional in situ measurements. However, these studies were of small waves (significant wave heights between 20 and 60 cm) and were taken from stationary nearshore platforms. Recently, innovations in the stereo methodology have led to its use in increasingly diverse conditions. For example, the work of Benetazzo et al. (2012) improved upon the image processing of Benetazzo (2006) and moved the system to an offshore platform, such that they measured significant wave heights greater than 2 m. As a further extension, Benetazzo et al. (2016) introduced a new ship-based stereo system, which is similar in many ways to the one described below.

In the last few years, researchers have used stereo wave measurements to explore a variety of scientific questions. For example, Sutherland and Melville (2013) used stereo-processed infrared imagery to estimate the dissipation of breaking waves, including microscale breakers, using the Duncan–Phillips scaling (Phillips 1985). Fedele et al. (2013) compared the wave statistics in space–time stereo images with nonlinear theoretical predictions. Most recently, Benetazzo et al. (2015) investigated the statistics of extreme waves, and Leckler et al. (2015) examined the shape of the full frequency–wavenumber spectrum in young wind waves.

We present measurements of open-ocean waves from a shipboard stereo video system installed on the R/V *Thomas G. Thompson* during a recent cruise to Station P in the North Pacific. We focus specifically on the geometry and steepness of open-ocean whitecaps. The paper proceeds as follows: Section 2 describes the stereo methodology, while section 3 validates the results against linear theory and in situ wave measurements. In section 4, the whitecaps are investigated in further detail. Section 5 provides discussion, and section 6 concludes. Note that all data and processing codes described below have been archived and are publicly available (http://hdl.handle.net/1773/38314).

2. Methods

a. Instrumentation

Measurements were made during a research cruise on board the R/V *Thomas G. Thompson* in the North Pacific Ocean. The ship departed from Seattle, Washington, on 27 December 2014 and returned on 14 January 2015, with the primary objective of replacing a moored wave buoy at Station P (50°N, 145°W). On several days the ship paused in the transit to hold station into the wind and collect measurements of the local wave conditions. The R/V *Thompson* is equipped with bow and stern thrusters and a dynamic positioning system, which allow it to keep a relatively stationary position even in rough seas. Conditions varied from quite calm (20-m wind speed $U_{20} < 1\,\mathrm{m\,s^{-1}}$, significant wave height $H_s = 1.3\,\mathrm{m}$) to large winter storms ($U_{20} = 23\,\mathrm{m\,s^{-1}}$, $H_s > 6.0\,\mathrm{m}$).

A stereo video system was installed for this cruise, which consisted of two Point Grey Flea2 cameras. The cameras were separated by 2 m along the rail just forward of the bridge, approximately 12 m above the mean sea surface, with a look angle approximately 12.5° below horizontal and orthogonal to the ship's rail. Identical systems were located on both the port and starboard sides, making it easy to switch sides depending on the position of the sun or clouds. Each stereo camera was equipped with a 9-mm fixed focal lens (leading to a roughly 30° horizontal field of view) and placed in a weatherproof housing. Each side had an additional Point Grey Flea2G camera recording a wider field of view (2.8-mm focal length). This camera was used heavily in Schwendeman and Thomson (2015b) for estimating whitecap coverage. It also kept the horizon in view in most frames, allowing for calculation of the camera pitch and roll as described in Schwendeman and Thomson (2015a). The port side cameras were mounted next to a Novatel combined inertial motion unit (IMU) and global navigation satellite system (GNSS), which measured the cameras' position and rotation.

While the ship held station with the stereo system recording, in situ measurements were made of the local wave spectra. Two varieties of drifting buoys were used, usually deployed at dawn and recovered at dusk. Datawell DWR-G4 Waveriders measured the horizontal wave orbital velocities with a GPS, from which the wave frequency spectrum $E(\omega)$, mean wave direction $\overline{\theta}(\omega)$, and directional spread $\Delta\theta(\omega)$ were calculated. The spectral calculations were made over 30-min intervals using Datawell's built-in processing (de Vries 2014). Meanwhile, custom-built Surface Wave Instrument Float with Tracking (SWIFT) drifters, described in Thomson (2012) and Thomson et al. (2016), used an onboard IMU to measure the buoy acceleration and orientation and produced frequency spectra and directional moments on 10-min intervals. The ship's sonic anemometer measured the true wind speed throughout the cruise at a height of roughly 20 m above the mean water line.

b. Stereo processing

Proper stereo video measurements require good synchronization and calibration of the cameras. Synchronization to within 10 μs was achieved by using a Point Grey IEEE 1394 (Firewire) hub, and the cameras were calibrated using the checkerboard routine included in MATLAB'S Computer Vision Toolbox. For the calibration procedure, a 10×5 array of 4″ black and white squares was shown to both cameras in their ship-mounted positions, which allowed the calibration algorithm to optimize both the extrinsic and intrinsic camera parameters. Prior to 1 January, the stereo cameras were run at 5 Hz; afterward the frame rate was set to 7.5 Hz. The Novatel IMU–GNSS data were recorded on a separate computer from the stereo imagery, which resulted in a small, unknown time offset between the two data streams. This was determined in postprocessing using a cross correlation of the time series of pitch and roll from the camera horizon method (Schwendeman and Thomson 2015a) with pitch and roll from the Novatel system. The IMU–GNSS data were then shifted to line up with the images.

The steps of the stereo image processing are outlined in Figs. 1 and 2 on a pair of images showing a large whitecap in the center of the field of view (this same example whitecap is also used in Fig. 8). The first step is stereo rectification, which is the process of transforming images such that pixel rows are epipolar lines. With the stereo cameras facing approximately parallel to one another, the rectification only slightly warps the images. The rectified images are shown in Figs. 1a and 1b. Next, the semiglobal algorithm from Hirschmuller (2008), as implemented in the MATLAB Computer Vision Toolbox, is used to calculate the disparity map, which is the image that maps pixels from the left rectified image to the right rectified image. Figure 1c shows the disparity result. The missing data on the left of the disparity map correspond to the region of the images that do not overlap.

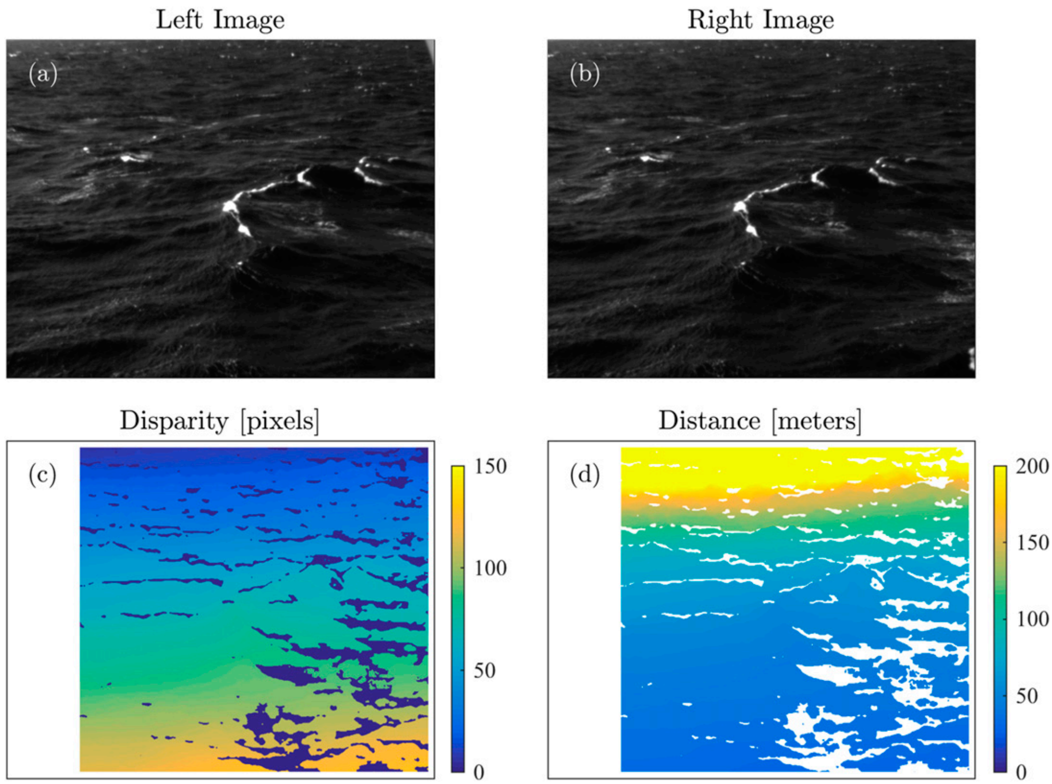

FIG. 1. An example showing (a),(b) a pair of rectified stereo images, (c) the resulting disparity map, and (d) the subsequent image projection. The left side of the disparity is cut off where the images do not overlap, and the holes in the disparity are where the confidence in the solution is low. The same example whitecap is shown in Figs. 2 and 8.

At each pixel in the left image, the matching pixel in the right image is the one that minimizes a cost function calculated over a window surrounding the pixels. The specific cost function used in the MATLAB implementation is the sum of absolute differences (SAD). The window size (called block size in MATLAB) can be chosen depending on the content of the images. A larger window produces a smoother disparity result but is less able to resolve sharp discontinuities. The MATLAB default block size of 15 pixels was found to work well for this data. The MATLAB disparity function reports subpixel disparities, rounded to the nearest 1/16, using the minimum of a parabola fit to the cost function calculated at integer pixel disparities.

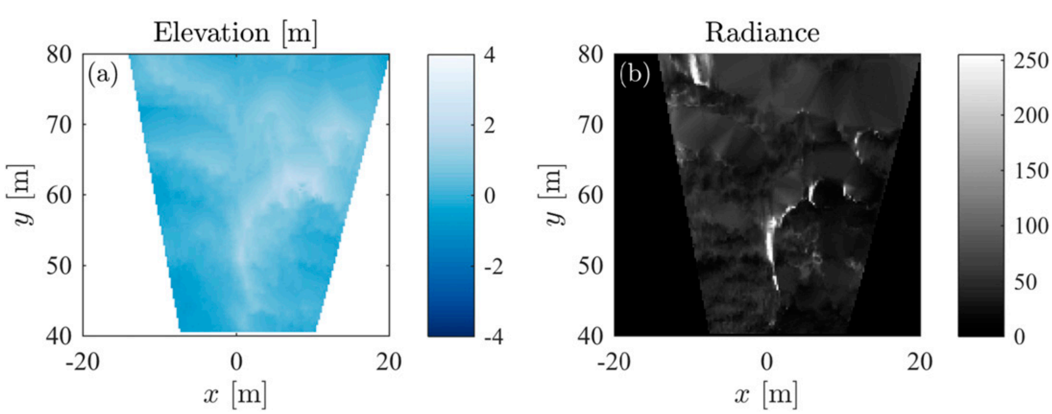

FIG. 2. The same example from Fig. 1, showing the (a) elevation and (b) radiance data products found by interpolating the stereo result onto a rectangular grid. These gridded products are later rotated such that the wind is in the $+x$ direction.

The uncertainty in the disparity image is related to the ability to positively identify matching pixels. The most uncertain points are generally those with less noteworthy features or low texture. MATLAB's implementation allows for several options to exclude the low-quality data. There is an unavoidable trade-off since excluding pixels leads to holes in the disparity map, but including more points results in errors and noise. Two filters were found to be helpful for removing bad points. The first is a contrast threshold. This sets a minimum contrast value for each pixel, where the contrast is computed through a convolution of the image with a Sobel filter. Less contrast indicates less texture around that particular pixel, and a threshold of 0.5 was found to work well here. Next, a uniqueness threshold identifies unreliable pixels by comparing the minimal value of the matching cost function with the second lowest value. Specifically, those pixels where the optimal value differed from the next best by less than 25% were discarded in the final disparity image. Finally, two median filters were applied to the data to reduce speckle noise. A 5-pixel square spatial median filter was applied to the disparity images, and a 3-frame temporal median filter was applied to the rotated and interpolated images (see below). The effect of these various quality control procedures is discussed further in section 3.

An example of the final disparity result is shown in Fig. 1c. At each pixel, the value of the disparity is inversely related to the range distance r of the sea surface to the camera:

$$r_{i,j} = \frac{f}{d_{i,j}}, \tag{1}$$

where f is the camera focal length, and $d_{i,j}$ is the disparity at pixel (i, j). Figure 1d shows the pixelwise distance image calculated from Eq. (1). The dominant signal is the tilt of the roughly flat sea surface relative to the oblique camera.

To observe the waves, the measurements are rotated into an Earth reference frame, in which the long-time mean sea surface is a plane at height zero with normal vector aligned with gravity. The rotation is performed using the synchronized IMU–GNSS data. Alternatively, Benetazzo et al. (2016) show that this rotation can be made by fitting a plane to each image; however, this method requires a large spatial field of view relative to the length of the waves. The data now make up a scattered point cloud, with each point corresponding to a pixel in the disparity map. The point cloud data are unstructured and difficult to analyze. Therefore, the final step is to interpolate the data onto a regular grid, as shown in Fig. 2.

A scattered, bilinear interpolation was performed on each image. Because of the rolling of the ship, the imaged area of the sea surface differed between frames. However, it was found that most images captured a region of the sea surface between 40 and 80 m from the ship. These were used as the limits of the gridded products. The grid spacing was chosen based on the resolution of the unstructured point cloud, which depends on the camera properties, the shape of the sea surface, and the distance from the ship. It is found that roughly 90% of points in the point cloud were within 25 cm of a neighboring point, and thus the grid spacing was chosen to be 25 cm.

The gridded elevation product (Fig. 2a) is heavily used in the following sections. Additionally, a similar interpolation can be performed on the original image pixel brightness values, resulting in an Earth-referenced radiance product, as shown in Fig. 2b. The radiance image looks blurred because the interpolation to a uniform grid tends to smear out the small, rough waves that provide much of the texture. However, the bright foam from whitecapping still shows up clearly, as seen in Fig. 2b. An additional translation and rotation is performed to bring the origin to the center of the field of view and the x axis in line with the average wind vector. Usually, the ship was pointed directly into the wind, such that this rotation is small. A video example of the rendered elevation/radiance products is included as supplemental material.

Although roughly 45 h of stereo video were taken, the data quality was highly variable due to variations in the natural lighting conditions and occasional rain; 10 video bursts stood out as the highest quality, and data products were calculated for their full durations, between 20 and 60 min each. A further 45 recordings were found to be of mostly good quality, from which 5 min each of video were processed. The remaining data were found to be too poor to warrant further examination and were not processed.

3. Comparison with wave buoys

The stereo wave measurements are first compared with the in situ measurements of the SWIFT and Waverider buoys. Although buoy wave measurements do not provide a perfect ground truth, measurement intercomparisons, such as Herbers et al. (2012), have shown them to be robust and consistent. For this comparison, each point in the gridded elevation product is processed as an independent time series (i.e., a virtual buoy). Frequency spectra $E(\omega)$ are calculated from the elevation time series at each point and averaged to a single spectrum for each video burst, from which the

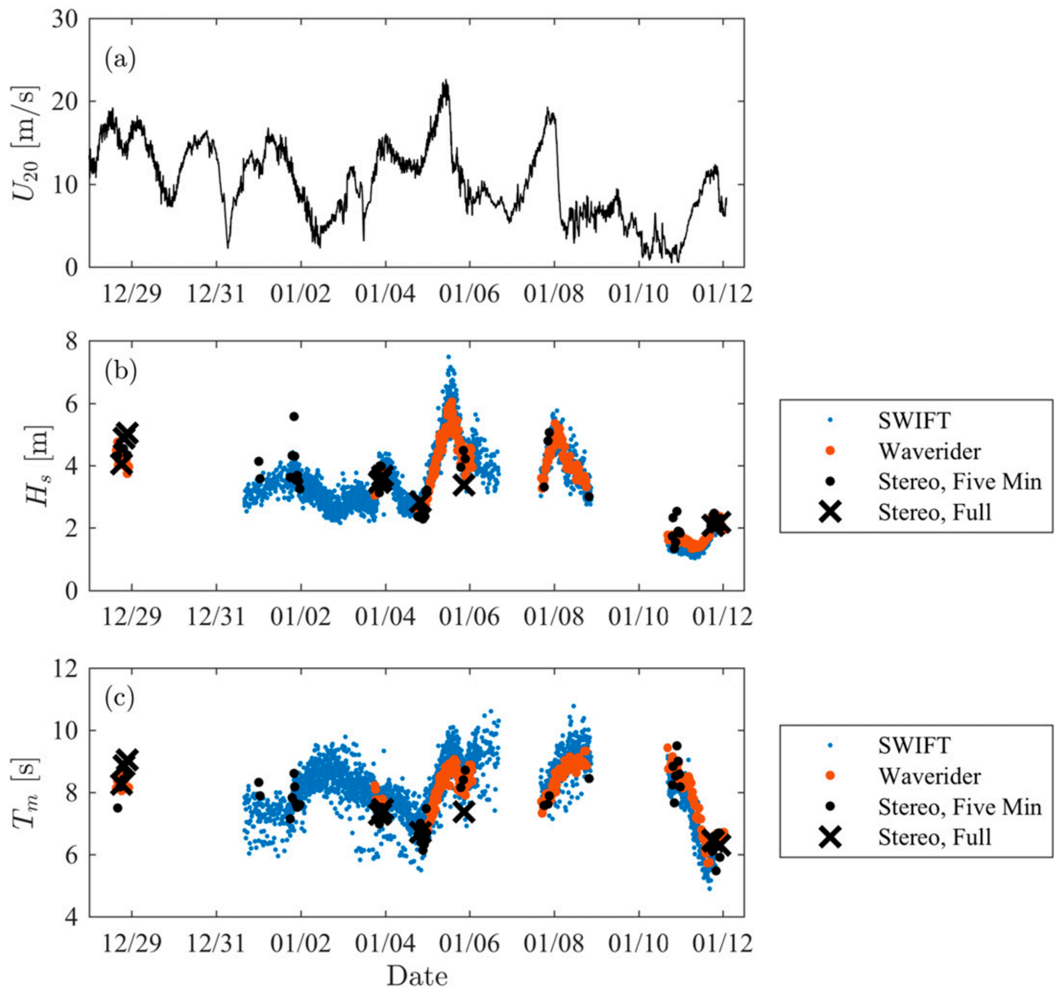

FIG. 3. Time series of (a) 20-m wind speed U_{20}, (b) wave height H_s, and (c) energy-weighted mean period T_m. The wind speed is measured from the ship, while the wave quantities are measured from SWIFT (blue) and Waverider buoys (orange) and from the stereo video (black circles = 5-min video segments, black x's = full video segments).

significant wave height $H_s = 4[\int E(\omega)\, d\omega]^{1/2}$ and energy-weighted mean wave period

$$T_m = \frac{2\pi \displaystyle\int E(\omega)\, d\omega}{\displaystyle\int \omega E(\omega)\, d\omega} \tag{2}$$

are calculated. These are plotted as a time series over the whole experiment in Fig. 3, along with the SWIFT and Waverider quantities when available. The time series show the wide range of conditions observed over the course of the experiment. During video recording, the buoys measured significant wave heights between 1.2 and 5.5 m and mean wave periods between 5.7 and 9.4 s. These measurements are subject to small amounts of uncorrected ship motion, including from surge and sway (RMS velocity fluctuation $\approx 0.3\,\mathrm{m\,s^{-1}}$), heading (RMS angle $\approx 2°$), and a small net drift (mean velocity $\approx 0.8\,\mathrm{m\,s^{-1}}$). Still, it can be seen that the stereo measurements follow the buoy data quite well overall, with only a few exceptions.

The stereo and buoy data are further compared in Fig. 4, showing scatterplots of H_s, T_m, and the mean wave steepness H_s/L_m (where L_m is calculated from T_m using the linear dispersion relation). Despite some scatter, the agreement is quite good between the two measurements. The H_s data agree quite well for wave heights up to about 4 m, but for larger waves the stereo measurements have the tendency to overestimate H_s relative to the buoys. Meanwhile, the T_m values show little overall bias. A similar comparison was made for the spectral peak period T_p (not shown), but apparent peak switching in the multimodal open-ocean spectra obscured the overall trends. The small scatter in H_s and T_m are amplified in the calculation of mean wave

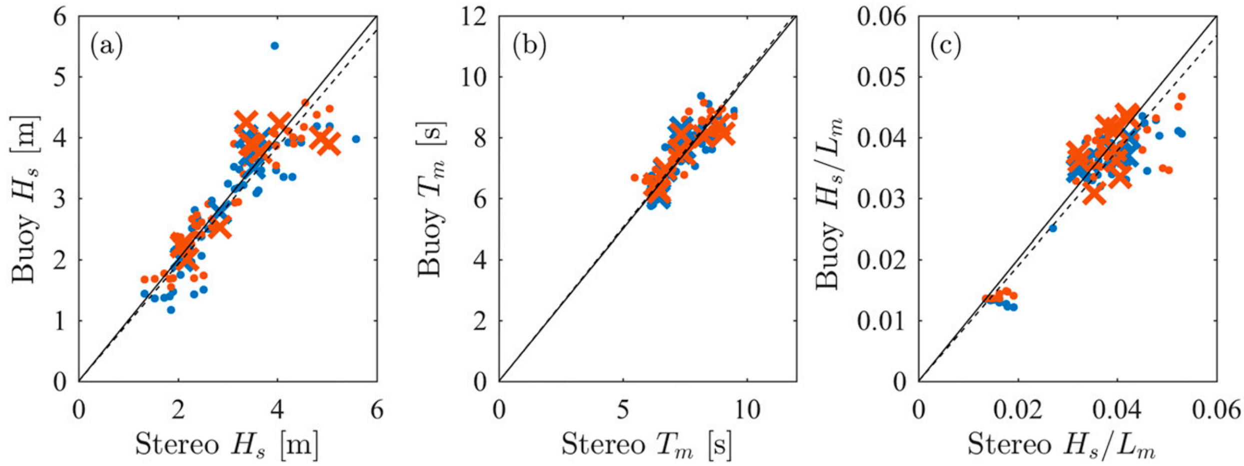

FIG. 4. Comparison of (a) significant wave height H_s, (b) mean period T_m, and (c) significant steepness H_s/L_m from the stereo video and buoys [SWIFT (blue), Waverider (orange)]. Circles are from the 5-min video segments, and x's are from the full video segments.

steepness. Despite this, the buoy and stereo measurements are still clearly consistent.

Three frequency spectra from the stereo video are compared to SWIFT and Waverider spectra in Fig. 5. These examples are drawn from the full video captures (crosses on Figs. 3, 4) from three different days (note that no SWIFT data are available for the 28 December example). The measurement times do not overlap exactly, as the Waverider spectra are calculated every 30 min, the SWIFT spectra are calculated every 10 min, and the stereo measurements last between 30 and 60 min. Plotted in gray are spectra from each stereo grid point, with the average spectra in black. Overall, the frequency spectra are similar in shape to those calculated from the buoy.

Although the spectral comparisons provide good validation for the stereo processing, they also point to some of the limitations of the stereo data. In the infragravity frequencies, the stereo spectra are considerably lower than the Waverider buoys. This could be due to the high-pass filter applied to the shipboard IMU–GNSS or a nonlinear effect from the buoys' Lagrangian motion (see Herbers and Janssen 2016). Regardless, the effect of this difference should be negligible, as these long-period motions are not of primary importance for the wave breaking.

At the higher frequencies, the spectra are expected to decay as a power law $S(\omega) \propto \omega^{-n}$, where n approximately equals 4 or 5 (see Banner 1990). Indeed, the stereo spectra show such behavior initially, but at larger frequencies noise begins to flatten the signal. This noise is likely related to small errors in the disparity calculations and in the linear interpolation of the data onto the rectangular grid. An examination of the sensitivity of the spectra to changes in the stereo processing (i.e., block size, contrast threshold, uniqueness threshold, and median filtering) reveal that the effects are largely confined to the high-frequency tail. In particular, the temporal median filter and uniqueness threshold tend to lower the noise floor when the data are of intermediate quality. For the 10 best video bursts examined in detail below (and from which the spectra of Fig. 5 are drawn), there is little sensitivity to these processing choices. The noise starts to be noticeable around roughly $5\,\mathrm{rad\,s^{-1}}$, corresponding to waves of 2.5-m wavelength.

Figure 5 also shows omnidirectional wavenumber spectra calculated from the stereo data for the same examples. To produce these curves, two-dimensional (k_x, k_y) wavenumber spectra are calculated at each video frame. The resulting (k_x, k_y) spectra are then averaged in time and interpolated onto a uniform directional grid of (k, θ), where $k = (k_x^2 + k_y^2)^{1/2}$ and $\theta = \arctan(k_y/k_x)$. The directional spectra are integrated over θ to yield the omnidirectional spectra $S(k)$. These direct measurements of the wavenumber spectra are compared with the frequency spectra transformed to wavenumber using linear dispersion with no current. Small differences are seen in the comparison between the directly calculated wavenumber spectra and the transformed frequency spectra, such as a small bump at the lowest wavenumbers and a slight overestimation in the high wavenumbers. These may be related to the limitations of calculating the discrete directional Fourier transform on a small, nonrectangular domain. Alternatively, they may be due to the secondary ship motions (small oscillations in surge, sway, and heading, plus a slow drift) or small surface currents, which introduce a Doppler shift in the frequency spectra that is not present in the wavenumber spectra.

Most importantly, the wavenumber spectra reveal the effect of the relatively small field of view of the cameras, which is between 20 and 40 m in the x direction

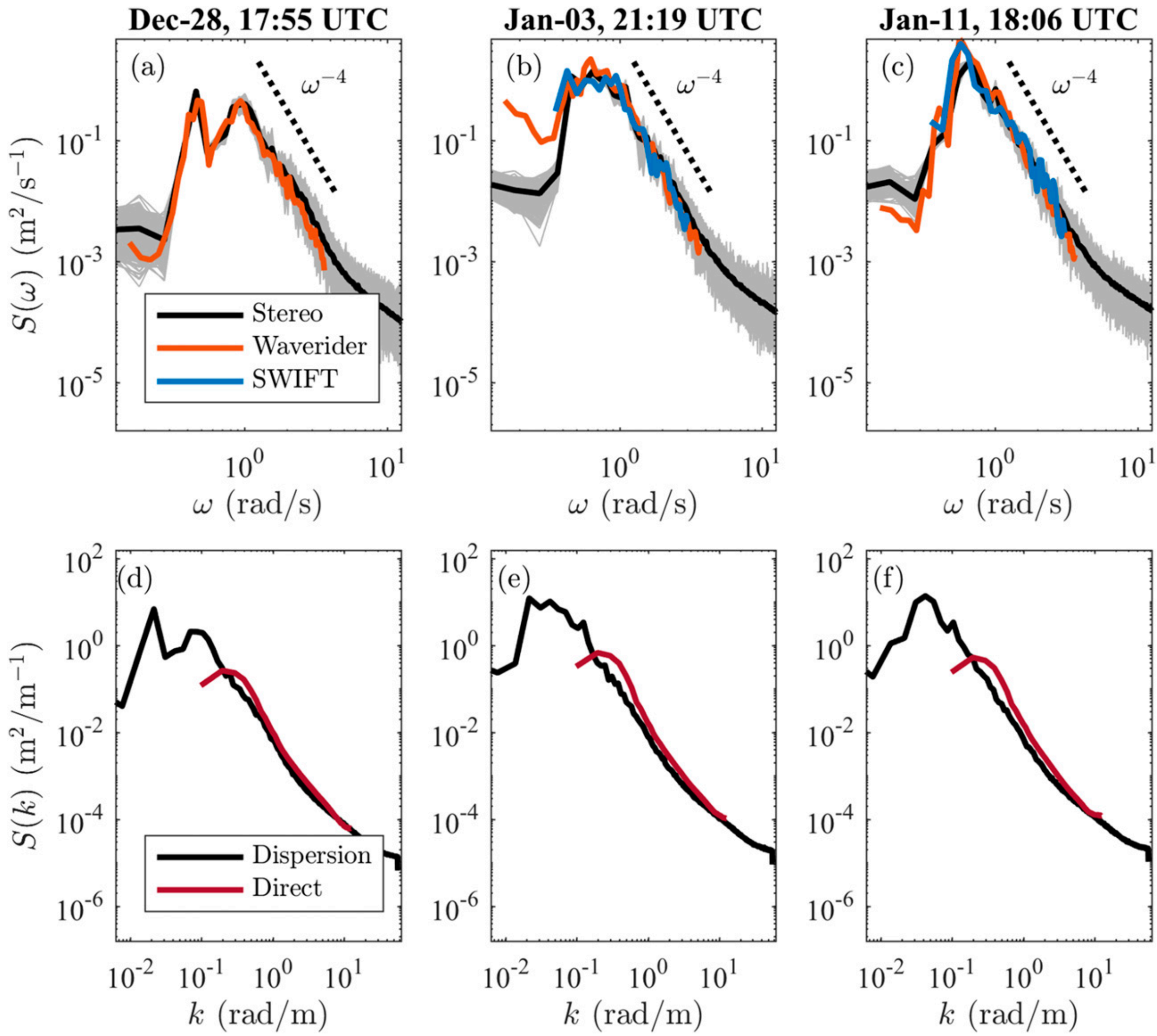

FIG. 5. Comparison of three wave spectra from three different days during the experiment. (a)–(c) Frequency spectra, measured from the SWIFT (blue), Waverider (orange), and stereo video. Gray lines are the spectra measured at each (x, y) in the stereo elevation product, with the black line as the average. (d)–(f) Omnidirectional wavenumber spectra, measured directly from the stereo video (red), and from the frequency spectra transformed using the linear dispersion relation (black). The wave spectra are most accurate for frequencies in the range of $0.2\pi \le \omega \le \pi$ rad s^{-1} ($2 \le T \le 10$ s period) and wavenumbers of $0.04\pi \le k \le 0.4\pi$ rad m^{-1} ($5 \le L \le 50$ m wavelength).

(depending on the range). The field of view does not resolve a full wavelength of the most energetic waves, which are between 50 and 200 m long. Fortunately, previous studies have shown that many of the breaking waves are shorter than the peak or dominant waves (e.g., Gemmrich and Farmer 1999). Still, the limited field of view does make certain analyses difficult or impossible, such as tracking the evolution of wave groups or estimating the dissipation from individual waves breaking. The spectra show that the region of best performance in the stereo data is for wave periods between 2 and 10 s and wavelengths between 5 and 50 m.

Finally, the probability density function (PDF) of the stereo surface elevation data is examined. PDFs are calculated over all x and y, and Fig. 6 shows the average for each of the 10 full videos. The elevations are expected to be quasi Gaussian (Forristall 2000), such that large deviations from a Gaussian distribution would indicate bias in the stereo data. In particular, because of the oblique camera angle, a major concern is occlusion, or shadowing, of the wave troughs in the far field by the crests in the near field. Figure 6 confirms that the surface elevations are near Gaussian to at least three standard deviations. Beyond this point, there is a noticeable

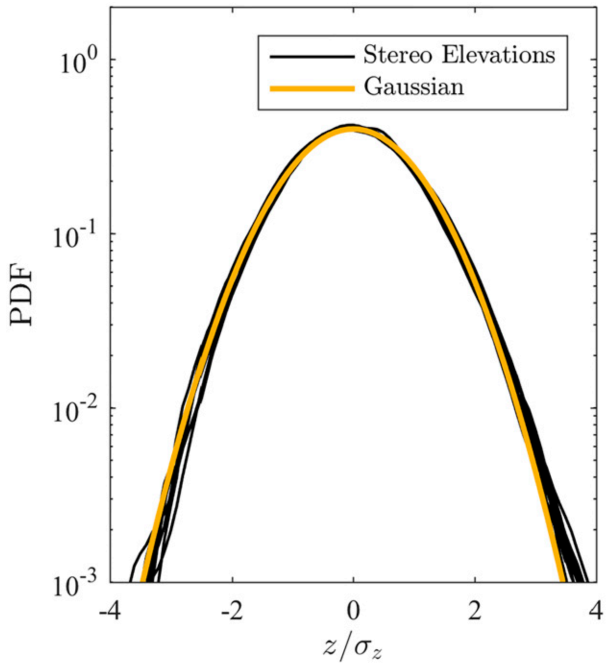

FIG. 6. The probability density function of surface elevation from the 10 full stereo video bursts (black), compared with a normal Gaussian distribution (yellow).

deviation from the Gaussian distribution, with more large positive elevations than low negative elevations. However, this is physically expected due to wave nonlinearity and is not necessarily indicative of measurement bias (Longuet-Higgins 1963). The plot is cut off where the statistics become less reliable, as the time scale of occurrence approaches the length of the video records. Overall, the effect of occlusion appears relatively small in the elevation PDFs.

In summary, evaluation of the stereo elevation product reveals the data to be statistically consistent with buoy measurements and linear wave theory. It also reveals some notable limitations. In particular, the small size of the field of view, the effect of noise on the high-frequency waves, and the small uncorrected ship motions must all be acknowledged. With this in mind, the following analysis of the wave breaking focuses on the prominent, intermediate length whitecaps, which are well resolved by the stereo measurements.

4. Results

a. Distributions of wave steepness (all waves)

Traditionally, estimates of wave steepness are only available from point measurements (e.g., buoys), meaning that the dispersion relation is needed to derive wavelength from a temporal signal. Most commonly, the average wave steepness is calculated from the frequency spectra as the significant wave height H_s, divided by a characteristic wavelength, such as the spectral peak wavelength L_p or energy-weighted mean wavelength L_m. Here, the characteristic wavelength is calculated in frequency space and transformed to a wavelength using the linear dispersion relation. Studies such as Holthuijsen and Herbers (1986) instead partition the time series of surface elevation into individual waves using a zero-crossing method, which allows a steepness $S_i = H_i/L_i$ to be estimated for each wave. Again, the wavelengths are not actually measured but calculated from the wave period using linear dispersion.

The stereo video data are uniquely suited for more direct estimates of steepness. Since the gridded elevation product also contains spatial information, the actual surface slope can be measured rather than inferred from dispersion. The magnitude of the surface gradient $|\nabla z(x, y)| = [(\partial z/\partial x)^2 + (\partial z/\partial y)^2]^{1/2}$ is calculated from the gridded elevation data using the central difference to approximate the partial derivatives.

Figure 7 shows how $|\nabla z(x, y)|$ relates to the steepness calculated from point measurements (using spectral or zero-crossing methods). First, Fig. 7a shows the probability density function (PDF) of $|\nabla z(x, y)|$, colored by the significant steepness H_s/L_m, as calculated from the stereo frequency spectra. It is clear that for larger H_s/L_m, the distribution of $|\nabla z|$ is also skewed higher. This is also seen in Fig. 7c, which shows a roughly linear relationship between H_s/L_m and the median gradient $\overline{|\nabla z|}$.

Normalizing the gradient by $\overline{|\nabla z|}$, as in Fig. 7e, shows that for moderate values of $|\nabla z(x, y)|$, the distributions are highly similar. The curves are well fit by the theoretical probability density function of slope derived by Liu et al. (1997):

$$P(|\nabla z|) = \frac{n}{n-1}\frac{|\nabla z|}{\sigma^2}\left[1 + \frac{|\nabla z|}{(n-1)\sigma^2}\right]^{-(n-2)/2}, \quad (3)$$

using $\sigma = 0.86\overline{|\nabla z|}$ and $n = 4.9$.

The observations show that above 2 to 3 times $\overline{|\nabla z|}$, the individual PDFs begin to diverge. Also shown is the fit to the data using $n = 2$ (the upper curve at large gradients) and $n = 12$ (lower curve), which also match the distributions in the low and moderate slopes but bracket the data at high slopes. For comparison, Liu et al. (1997) found that the measurements of Cox and Munk (1954) could be fit using a range of $6 \le n \le 100$. Physically, large values of n indicate a narrow distribution of the wave frequency. As discussed in Babanin (2011), the frequency bandwidth is related to the modulational properties of the dominant waves (i.e., the wave groups). Thus, the probability of large surface

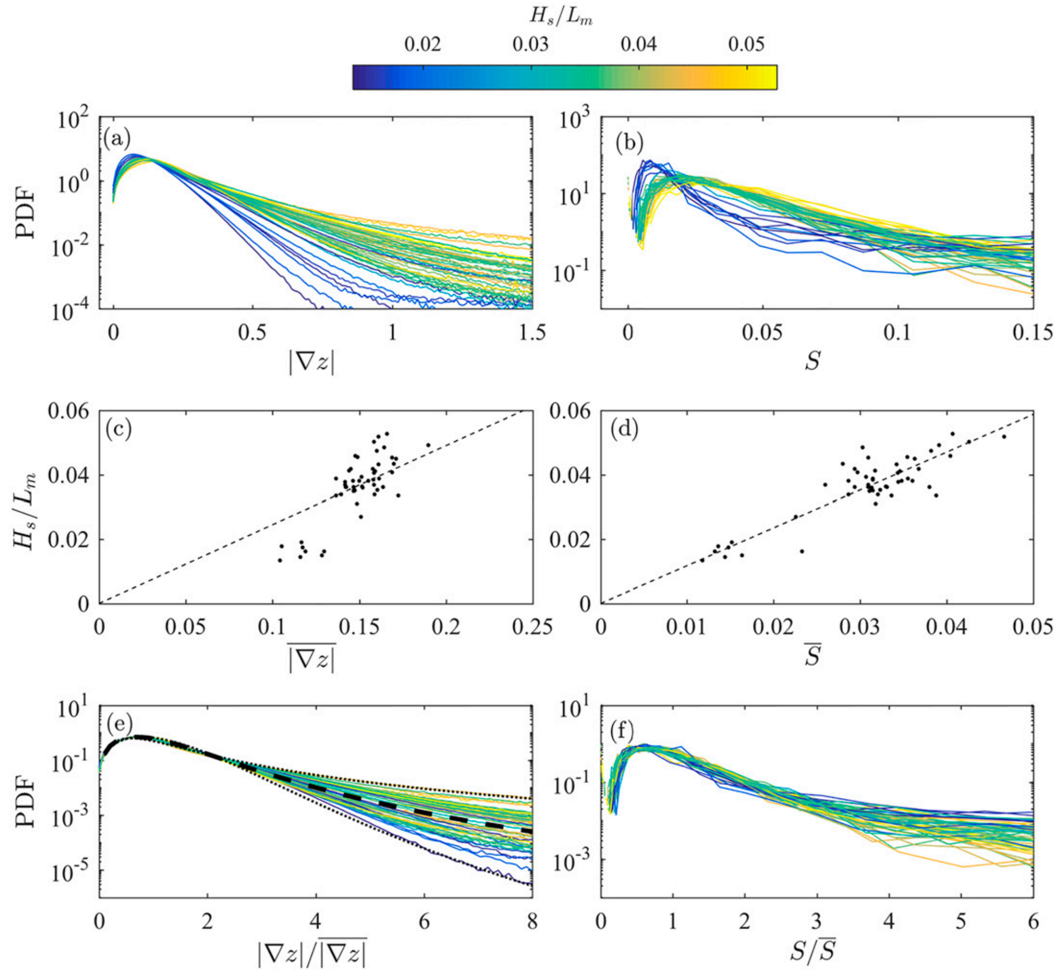

FIG. 7. PDFs of (a) surface gradient magnitude $|\nabla z|$ and (b) wave steepness from zero down crossings S, each colored by significant steepness H_s/L_m. (c),(d) H_s/L_m plotted against the median values of $|\nabla z|$ and S. (e),(f) The PDFs scaled by their median values. The dashed line in (e) corresponds to the theoretical distribution of Liu et al. (1997) with $\sigma = 0.86\overline{|\nabla z|}$ and $n = 4.9$. Dotted lines are fits using $n = 2$ (upper curve at large $|\nabla z|$) and $n = 12$ (lower curve).

slopes increases (n becomes smaller) when wave groups are pronounced (larger frequency bandwidth). Additionally, this model assumes independent distributions of wave height and wave period. As discussed in Liu et al. (1997), deviations from this assumption increase the probability density of high surface slopes, which can be reproduced by decreasing n.

The distribution of wave steepness is also shown using a zero down-crossing method, as in Holthuijsen and Herbers (1986). Specifically, elevation time series are made from (x, y) points taken every 5 m, resulting in 81 virtual wave gauges (although several have no data because of the shape of the field of view). In each time series, waves are identified as lying between the two nearest points where the elevation crosses from positive to negative. For each wave, a steepness S is calculated as the difference between the maximum and minimum elevation, divided by the estimated wavelength, using linear dispersion and the period between down crossings. Figure 7b shows the PDFs of S, again colored by H_s/L_m. It should be noted that the zero-crossing method is not ideal for these broadband waves, where short waves riding on long waves may fully lie below or above the mean water line.

Still, as with the surface gradient, Fig. 7d reveals that the median wave steepness $\overline{S}$ is linearly related to H_s/L_m, and Fig. 7f shows that the distributions are largely similar after scaling by $\overline{S}$. The main difference in using the zero-crossing steepness S is that each wave is assigned a single value of steepness, whereas the surface gradient magnitude $|\nabla z|$ captures variations in the instantaneous and local wave slope. The increase in data causes the

PDFs of $|\nabla z|$ to be much smoother than those of S. Additionally, the PDFs of $|\nabla z|$ show a clear signal near the tail of the distribution, which is not visible in the PDFs of S (although there is an apparent noise floor that becomes obvious in the least steep conditions). This is consistent with the hypothesis of Liu et al. (1997), who argue that the variation in the shape of the $|\nabla z|$ distribution is a nonlinear effect, which would not be captured by the zero-crossing method.

b. *Distributions of wave steepness (whitecaps)*

Are the extreme surface slopes related to the wave breaking? To answer this question, the radiance data product (Fig. 2b) is thresholded to isolate the whitecap foam. The thresholding is performed using the method of Kleiss and Melville (2011). This gives a three-dimensional array of Boolean values $W(x, y, t)$, in which a value of 1 indicates the presence of whitecap foam. However, W does not distinguish between the recently formed foam from active breaking and the decaying foam left behind from past breakers. Therefore, another variable $\Delta W(x, y, t)$ is used, which more closely follows the active breaking. This was introduced in Schwendeman and Thomson (2015b) and is calculated from W by simply negating pixels in W for a period of several seconds after they are initially flipped from 0 to 1. Since the residual whitecap foam tends to remain mostly stationary, these pixels are ignored in ΔW. Figure 8 demonstrates this thresholding as applied to the whitecap of Fig. 2.

The PDFs in Fig. 7 were cut off at high steepness, where noise contamination became apparent in several of the 5-min video segments. To isolate the relationship of wave steepness to wave breaking, it is necessary to focus on the highest-quality data. Thus, for this and the remainder of the paper, the data come from only the 10 best-case video segments, each lasting between 20 and 60 min.

Figure 9 compares the probability density of $|\nabla z|$ in the whitecap ($\Delta W = 1$) and nonwhitecap ($\Delta W = 0$) pixels. The distribution of the whitecaps skews high, indicating that the active whitecap foam is clustered near regions of high surface slope. This is best seen in Fig. 9b, which plots the ratio of the two probability distributions. The whitecap pixels are up to an order of magnitude more likely than the nonwhitecaps to occur at large gradients in the surface elevation, and the ratio peaks around $|\nabla z| \approx 1.25$. In contrast to the wave-by-wave analysis of Holthuijsen and Herbers (1986), this suggests a distinct difference in the geometry of the breaking waves. The disagreement is likely due to the use here of the local surface slopes, as opposed to the bulk steepness in Holthuijsen and Herbers (1986).

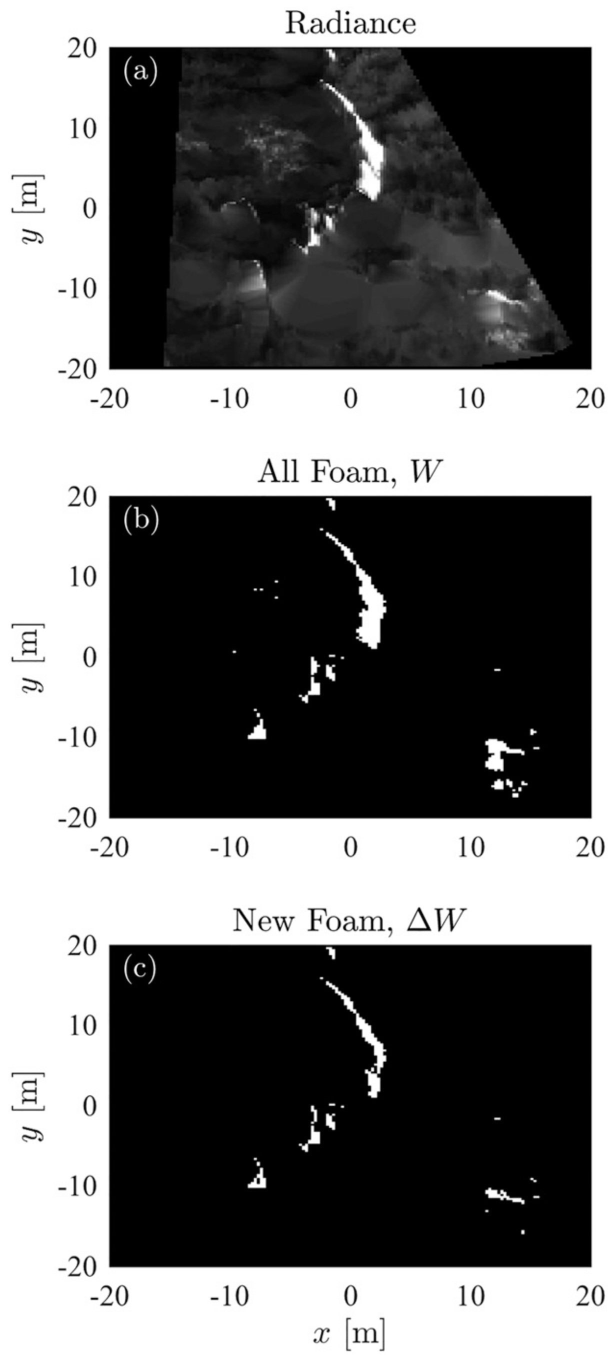

FIG. 8. Example showing the thresholding procedure, as applied to the whitecap of Figs. 1 and 2. (a) The raw radiance product. (b) Result after thresholding using the method of Kleiss and Melville (2011). (c) Further isolating only new whitecap foam, as described in Schwendeman and Thomson (2015b).

c. *Whitecap profiles*

To better understand the shape of the breaking waves, the clearest whitecap events are identified for further examination. This is not straightforward, partly because

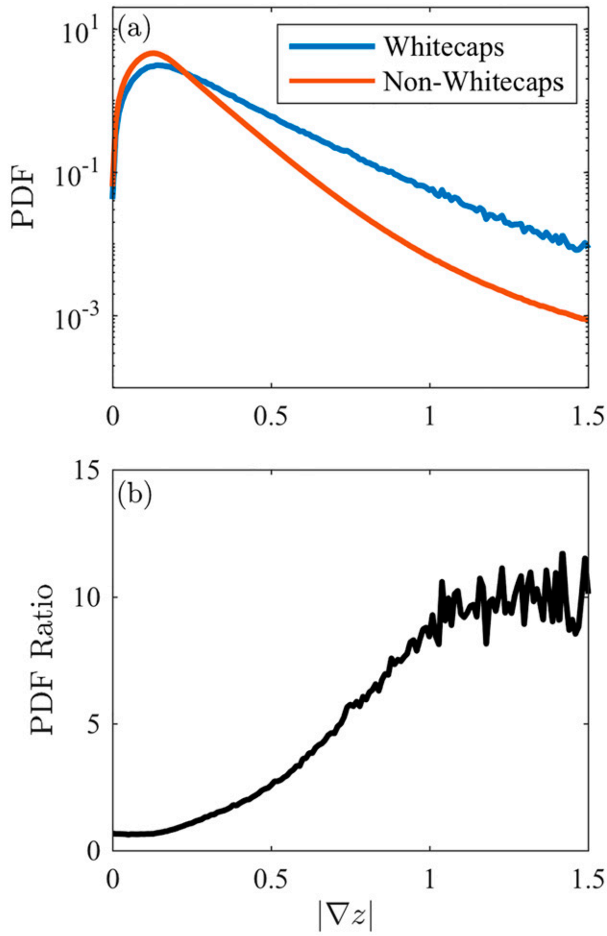

FIG. 9. (a) The probability distribution function of surface gradient magnitude $|\nabla z|$ separated by whitecap (blue) and nonwhitecap (orange) pixels. (b) The ratio of the two PDFs.

the whitecap foam does not always stay connected through the breaking process, often separating into several groups of pixels. Additionally, although the new whitecap foam is a better proxy for active breaking, the definition of $\Delta W(x, y, t)$ prevents the whitecaps from overlapping between frames. To correct both issues, a topological dilation is applied to the binary $\Delta W(x, y, t)$ array. The dilation step essentially connects all whitecap pixels within 1 m of each other in the current, preceding, or following frames. Each group of spatially or temporally connected pixels in the dilated $\Delta W(x, y, t)$ is considered as a potential whitecap event. A minimum duration of 2 s is used to avoid transient events (often on the boundary of the field of view) or noise (often from advected residual foam). Over the lifetime of each whitecap event, the grouped pixels are approximated by an ellipse with major axis L_{major}, minor axis L_{minor}, centroid x_c and y_c, and orientation θ. The ratio of L_{major} to L_{minor} is found at each time, and the time when this ratio is maximum is recorded as $t_1 = 0$. The best cases are identified as those where the maximum $L_{\mathrm{major}}/L_{\mathrm{minor}}$ is greater than 4, when θ is within 45° of the wind direction, and the (x_c, y_c) is within 10 m of the center of the field of view. These conditions eliminate cases of noise and advected foam, ensure that the breaking wave is sufficiently long crested to determine a principal axis, and avoid breakers occurring near the edge of the field of view. A somewhat similar procedure for identifying distinct whitecap events in visual imagery was described in Gemmrich et al. (2008). This results in 137 potential whitecap events, which are checked manually to be sure they show unambiguous active breaking, after which 103 examples remain.

Next, a local coordinate system is defined around the breaking crest at $t_1 = 0$, with x_1 and y_1 coordinates orthogonal and parallel to the major axis of the whitecap, respectively. The spatial origin $(x_1, y_1) = (0, 0)$ is found as the point of maximum z, within ± 2.5 m of the whitecap centroid (x_c, y_c). Profiles of z at $y_1 = 0$ are interpolated onto x_1 for $-30 \le t_1 \le 30$ s.

A Hilbert transform is applied to the wave profiles to calculate the evolution of the whitecap frequency, wavenumber, and amplitude. The Hilbert transform produces an analytic function that defines a local amplitude and phase for the wave signal $z(x_1, t_1) = \Re\{A(x_1, t_1)\exp[i\phi(x_1, t_1)]\}$. The transform can be performed in space or in time, such that there are actually two amplitude and two phase functions: $A_x(x_1, t_1)$, $\phi_x(x_1, t_1)$, and $A_t(x_1, t_1)$, and $\phi_t(x_1, t_1)$ (see Stansell and MacFarlane 2002). Differentiating ϕ_x in x_1 gives a local and instantaneous wavenumber $k(x_1, t_1)$, while differentiating ϕ_t in t_1 gives a local and instantaneous frequency $\omega(x_1, t_1)$. It should be noted that wavelet analysis may provide an alternative way to determine local wavenumber and frequency, as in Liu and Babanin (2004).

Figure 10 shows the ensemble average of the whitecap profiles and Hilbert transform results. All values are normalized, using an average wavenumber $\overline{k}$, frequency $\overline{\omega}$, and amplitude $\overline{A_x}$ or $\overline{A_t}$ from the Hilbert analysis. Since ω, k, A_x, and A_t each vary over the domain, their mean value is somewhat sensitive to the choice of x_1 and t_1 limits. Here, the mean is found between $-10 \le x_1 \le 10$ m and $-3 \le t_1 \le 3$ s, which encompasses the bulk of the breaking wave but avoids noise near the edge of the domain. These averages were found to agree well with the wave amplitudes and periods from a zero-crossing analysis (not shown). The scaling of the wave elevation is performed after first subtracting the mean surface elevation of the profile, over the same limits.

Analysis of the ensemble-averaged breaking wave profiles is similar to the processing of laboratory wave data. Figure 10a shows the wave moving in the positive

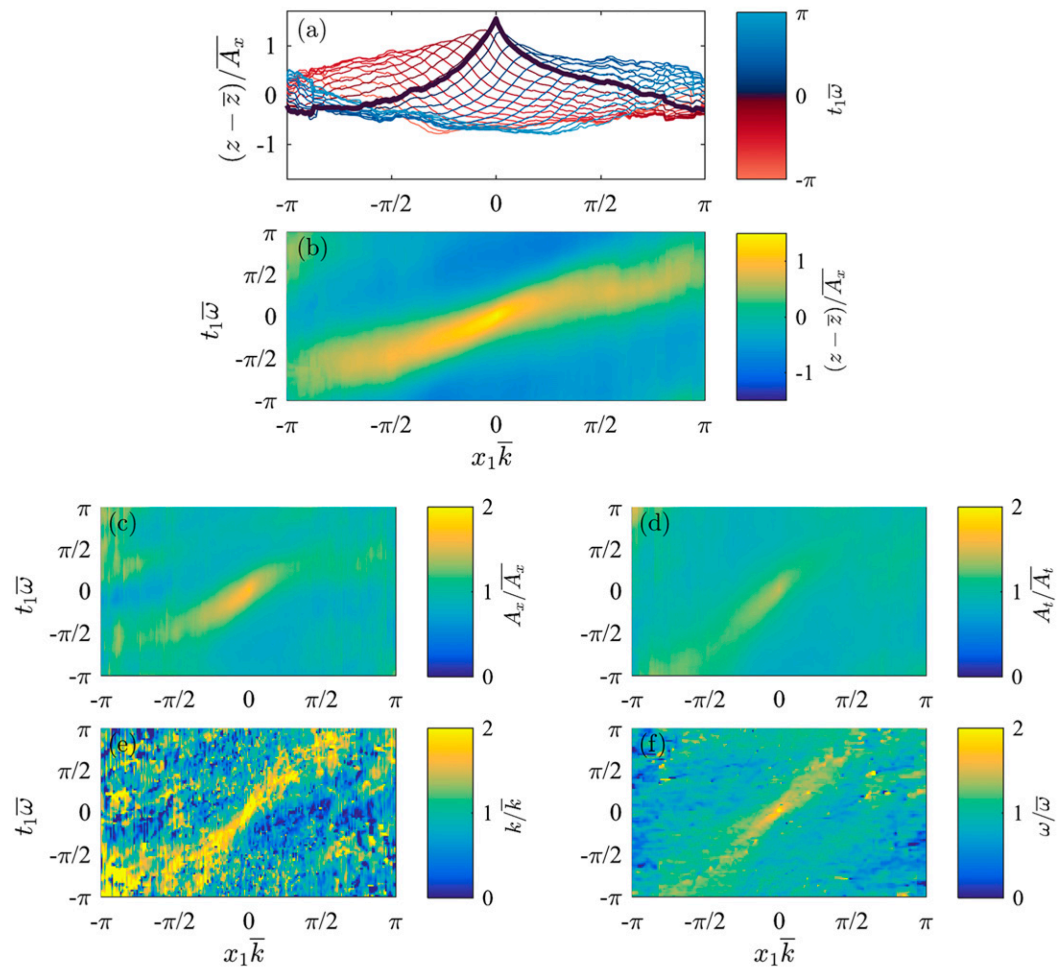

FIG. 10. Ensemble averages of the 103 whitecap profiles and Hilbert transform results, normalized by the individual mean values over $-10 \le x_1 \le 10$ m and $-3 \le t_1 \le 3$ s. (a),(b) Two views of the elevation profiles $(z - \overline{z})/\overline{A_x}$, (c) the local spatial amplitude $A_x/\overline{A_x}$, (d) temporal amplitude $A_t/\overline{A_t}$, (e) wavenumber $k/\overline{k}$, and (f) frequency $\omega/\overline{\omega}$.

x_1 direction as time progresses (colors changing from red to blue). The breaker appears very smooth, which is the product of averaging over the 103 individual waves. There is a clear steepening and sharpening of the wave crest, which quickly relaxes after breaking. The maximum in slope occurs very near the breaking crest but is not symmetric. Initially the maximum slope is on the front face, but after breaking it is on the back side. The wave is also vertically asymmetric. At the break point, the breaker lies almost fully above the mean water line. After breaking, the wave begins to shift to a lower mean elevation. The same information can be alternatively presented as a timestack, as in Fig. 10b. Unfortunately, the limited spatial field of view means that the wave is less well sampled as $x_1\overline{k}$ approaches π and $-\pi$.

Whereas the Hilbert transform of a monochromatic sinusoidal waveform yields a constant amplitude, wavenumber, and frequency, this is not the case for these breaking waves. Instead, there is a localized increase in the wave amplitude, wavenumber, and frequency near the wave crest. Thus, the ensemble-averaged Hilbert transform results show a rapid increase in local crest steepness as the whitecap occurs. This is shown in Fig. 11, where the instantaneous steepness is plotted as A_xk. At the break point, $(x_1, t_1) = (0, 0)$, the mean local steepness is 0.42. For comparison, the mean steepness averaged over the full period and wavelength is 0.15.

The change in the shape of the breaking waves, in particular this local steepening near the crest, is shown explicitly in Fig. 12. The normalized profiles are plotted at $t_1\overline{\omega} = -\pi/4, 0,$ and $\pi/4$, along with the ensemble-averaged profile. For reference, they are compared with the Stokes limiting wave, using the one-term approximation from Rainey and Longuet-Higgins (2006). Again,

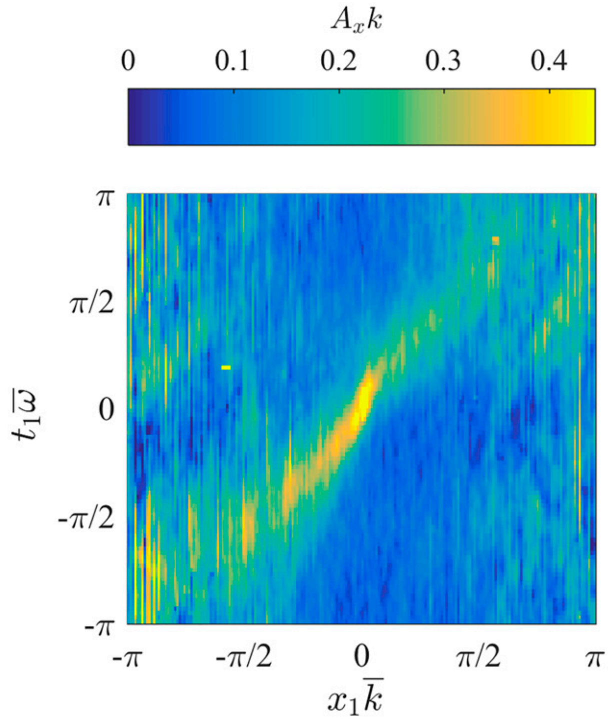

FIG. 11. Ensemble-averaged local wave steepness $A_x k$ from the Hilbert transform.

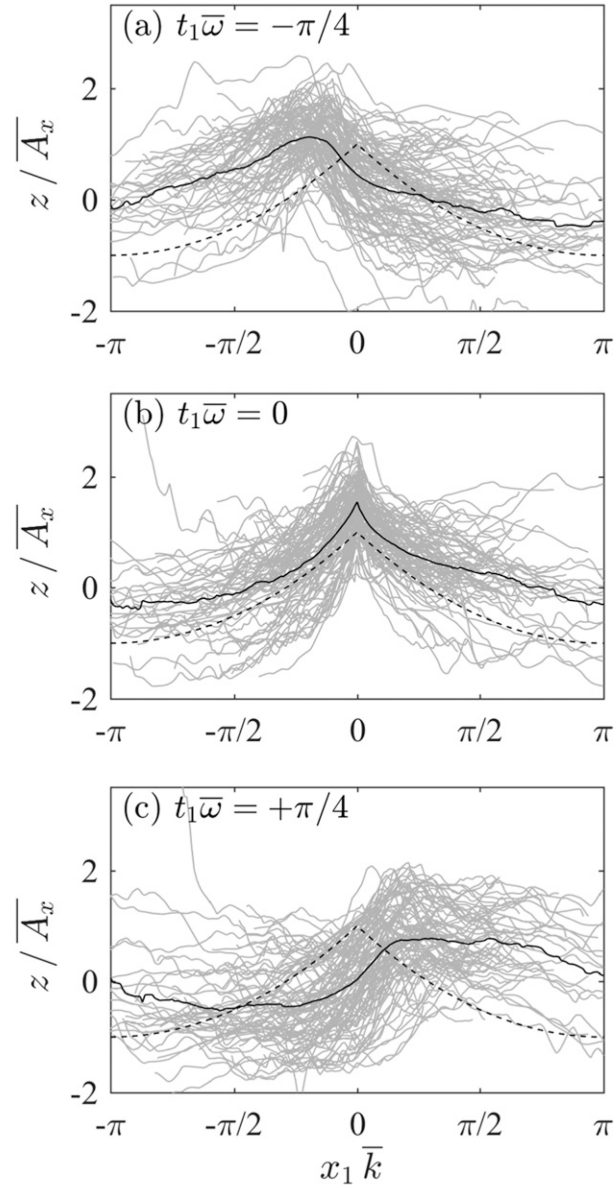

FIG. 12. Breaking wave profiles, scaled by the average spatial amplitude $\overline{A_x}$ and wavenumber $\overline{k}$ from the Hilbert analysis. The progression is shown from $t_1\overline{\omega} =$ (a) $-\pi/4$ to (b) 0 to (c) $+\pi/4$. The solid line shows the ensemble-averaged profile, while the dashed line shows the one-term Stokes limiting wave approximation from Rainey and Longuet-Higgins (2006).

the change in asymmetry is apparent before and after the break point. In just a quarter period, the forward tilt of the crest (at $t_1\overline{\omega} = -\pi/4$) has transitioned to a backward lean (at $t_1\overline{\omega} = +\pi/4$). Throughout the progression, the individual profiles show much scatter, as is expected in broadband waves. However, at the crest of the wave near the break point, the profiles closely resemble the angular crest of the Stokes wave. This maximally steep crest feature quickly dissipates upon breaking, to the point where it is no longer visible at $t_1\overline{\omega} = +\pi/4$.

Finally, the propagation speeds of these breaking crests are examined. Banner et al. (2014) showed that the steepest crests of nonlinear wave groups propagate significantly slower than the predicted linear or weakly nonlinear phase speeds. This behavior is also seen in the whitecap profiles, as shown in Fig. 13. The true wave phase speeds c are calculated as the ratio of the average frequency and wavenumber, which are independently measured from the Hilbert transform. These are compared with the phase speeds calculated from the average frequency using the linear dispersion relation c_0. Although there is significant scatter, the true phase speeds are almost uniformly less than the linear phase speed. A fit to this data gives $c = 0.61c_0$, consistent with the field measurements of Banner et al. (2014) showing $c \approx 0.61c_0$. This suggests that these whitecaps formed near the center of nonlinear wave groups.

5. Discussion

a. Comparison with previous measurements

Previously, studies such as Holthuijsen and Herbers (1986) have shown oceanic breaking waves to be of similar steepness to their nonbreaking counterparts and much less steep than the Stokes limit. Here, by contrast, Figs. 9, 11, and 12 suggest that breaking is associated with high steepness and that breaking waves do

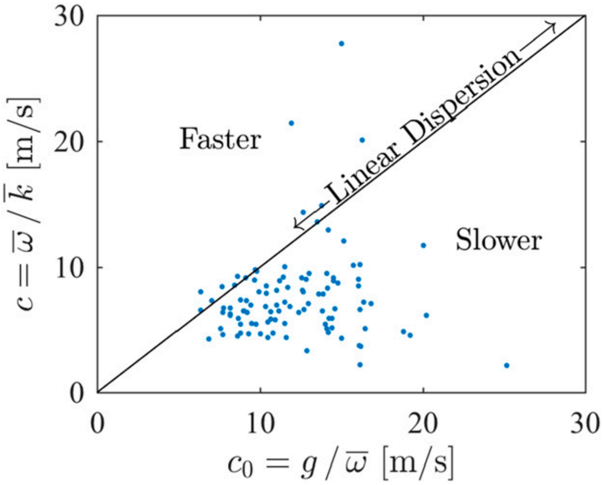

FIG. 13. Comparison of measured phase speed c with linear phase speed c_0 from the Hilbert transform analysis. The solid line is the 1:1 line, indicating perfect linear dispersion.

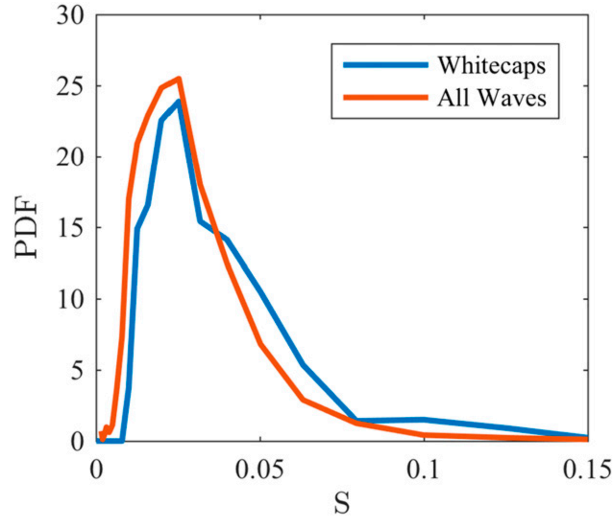

FIG. 14. PDF of wave steepness for the breaking wave profiles from a zero-crossing analysis, compared with the overall steepness PDF from a weighted average of the curves in Fig. 7. These PDFs are consistent with the results of Holthuijsen and Herbers (1986) but obscure the locally steep crest features seen in Figs. 11 and 12.

resemble the corner crest of a Stokes limiting wave. The apparent contradiction with previous measurements is in part because these steep crests are highly localized, such that they are not often accompanied by the full limiting wave profile. Thus, the whitecaps do not appear particularly steep when examined using bulk metrics. This is shown explicitly in Fig. 14, which compares the probability density of wave steepness from the whitecap profiles with the overall steepness distribution, using a weighted average of the curves in Fig. 7 based on the number of whitecaps from each video burst. This zero-crossing method is taken directly from Holthuijsen and Herbers (1986), and the results are very similar to theirs. Indeed, in a bulk sense, the whitecaps are not considerably steeper than the nonbreaking waves.

Furthermore, the steepness measurements from the zero-crossing method of Holthuijsen and Herbers (1986) rely on assuming a wave phase speed from linear dispersion, which Fig. 13 definitively shows is not applicable. Since the phase speed is actually lower than suggested by linear dispersion, the true bulk steepnesses are higher than the estimates from a time series measured at a point. Specifically, if the phase speed is actually 25% less than the linear expectation, as in Banner et al. (2014), the true wave steepness is 33% larger than what is estimated from the time series.

Babanin et al. (2010) suggests that the reason field measurements often show whitecapping at relatively low steepness is that the maximum steepness occurs prior to the detection of whitecap foam. The data do not show evidence of this time delay effect (see Fig. 12). Still, the point holds; determining the actual onset of breaking in field data is a challenge. The presence of new whitecap foam does indicate active breaking, but the distinction between new foam and residual foam is often unclear. In making two-dimensional profiles of whitecaps, it was found that the surest way to identify active breaking was to use the aspect ratio of the foam patch. Still, manual inspection of these best cases removed roughly 25% of the tagged profiles, which were either ambiguous or mislabeled breaking events. Furthermore, foam from small breaking events often does not show up as brightly as from large events or even at all in the case of microbreaking waves. The identification of breaking from whitecap foam is therefore one of the largest sources of uncertainty in these observations.

b. The role of nonlinearity

What physical mechanism is responsible for the localized increase in wave steepness in the breaking waves? Babanin (2011) divides potential steepening mechanisms into two categories: instability mechanisms and superposition mechanisms. The Benjamin–Fier instability, more generally called modulational instability, is a nonlinear effect that leads monochromatic wave trains to dissolve into modulating wave groups and can eventually lead to breaking [see the review of Yuen and Lake (1980)]. Conversely, superposition mechanisms are primarily linear effects, which produce high steepnesses by focusing two or more wave crests of different directions (directional focusing) or phase speeds (dispersive focusing).

Our measurements indicate that nonlinear group dynamics are critical in producing the necessary steepnesses

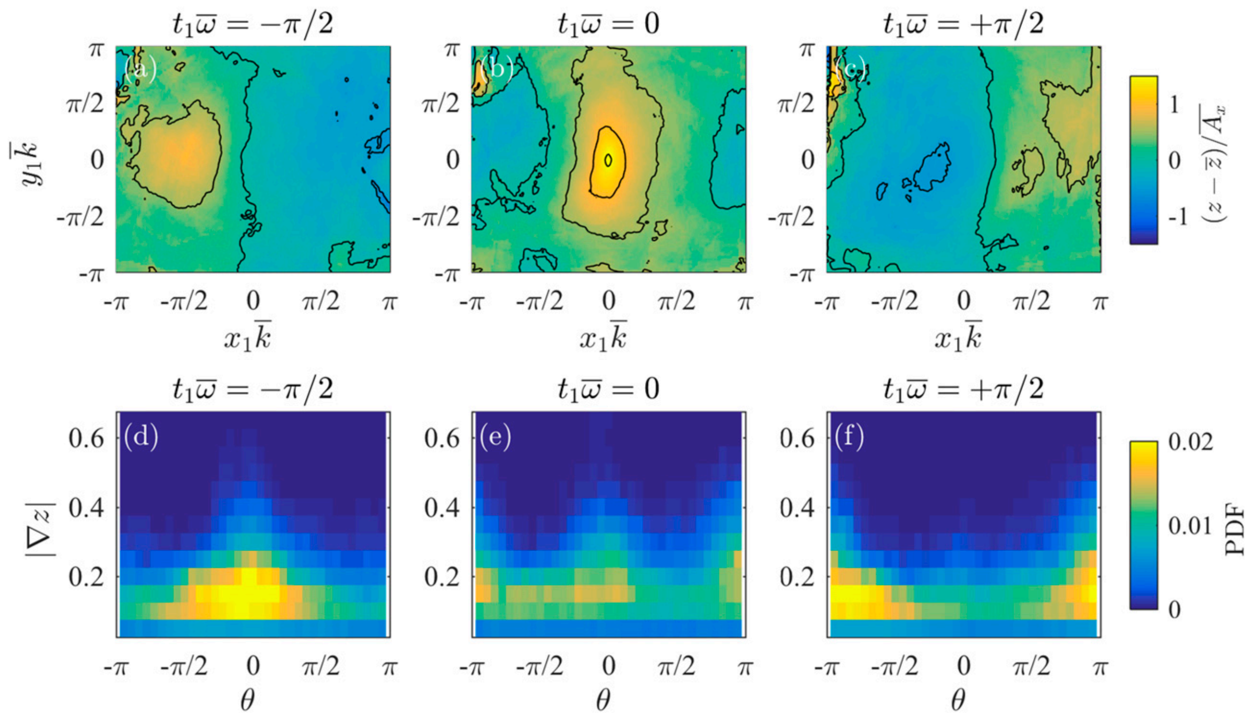

FIG. 15. Ensemble average of the 103 whitecaps in two dimensions at times $t_1\overline{\omega} =$ (a) $-\pi/2$, (b) 0, and (c) $+\pi/2$. As before, all the waves were first normalized by the average wavenumber $\overline{k}$ and amplitude $\overline{A_x}$ from the previous section. (d)–(f) The joint PDF of surface gradient magnitude $|\nabla z|$ and direction θ for the whitecaps over the same times. Here, $\theta = 0$ $(\pm\pi)$ corresponds to downward slopes in the $+x_1$ $(-x_1)$ direction.

for breaking to occur. Figure 9 shows that breaking often occurs near points of locally extreme surface slope. Meanwhile, Fig. 7 shows that the probability of these extreme surface slopes (at the tail of the distribution) is highly variable, which Liu et al. (1997) attribute to nonlinear effects. Furthermore, the breaking wave profiles display many of the characteristics associated with nonlinear wave groups. For example, the asymmetry of the profiles, in which the wave tilts forward prior to breaking and backward after, was predicted by the theoretical work of Tayfun (1986). Similarly, the reduced phase speed of the breaking crests, shown in Fig. 13, is likely due to the nonlinear group dynamics described in Banner et al. (2014).

By contrast, there is not much evidence for breaking due to superposition. In particular, the wave profiles and their Hilbert transforms do not show steepening from long waves overtaking short waves, as in dispersive focusing. Instead, they show steep nonlinear waves propagating as a phase-locked signal. This matches the hypothesis of Babanin (2011), which argues on probabilistic grounds that dispersive focusing alone cannot produce the amount of breaking measured in natural wavefields. It should be noted that linear superposition may be responsible for producing the initial moderately steep waveform, at which point the nonlinear dynamics become dominant and lead to breaking.

The breaking wave profiles along a principal axis cannot address the question of directional superposition, so this linear mechanism remains a viable hypothesis. Figure 15 shows again an ensemble average of the 103 breaking waves, this time retaining both x_1 and y_1 spatial dimensions. Both x_1 and y_1 are scaled by the average wavenumber $\overline{k}$ from the previous analysis. Snapshots of the two-dimensional waveform are shown at $t_1\overline{\omega} = -\pi/2$, 0, and π (i.e., at the break point and a quarter period before and after). In addition, the joint PDF of surface gradient magnitude $|\nabla z|$ and direction θ are shown for the same times. Here, $\theta = 0$ corresponds to downward slopes in the $+x_1$ direction, and $\theta = \pm\pi$ indicates downward slopes in the $-x_1$ direction. Because of the limited spatial domain, they are not symmetric before and after breaking, when the wave is entering and leaving the field of view.

These plots show no indication of breaking from directional focusing, at least it is not common enough to not be visible in the ensemble averages. Both the wave motion and the direction of the largest surface slopes are primarily in the x_1 direction, which validates the use of the principal axis wave profiles in the previous section. Still, the two-dimensional shape of the average whitecap is interesting; for example, the progression shows the wave spreading somewhat in the y_1 direction during breaking. Moreover, these plots provide further evidence of the highly localized and transient nature of the steep whitecap crests. This three-dimensionality of the breaking crests may be a topic for further research.

6. Conclusions

The stereo data provide a unique spatiotemporal measurement of the breaking wave geometries. To summarize some of the key findings:

- The probability distribution functions suggest that whitecaps often occur near extremes in the surface slope (Fig. 9).
- The profiles of breaking waves are characterized by transient, locally steep crests, which resemble the Stokes limiting corner crest (Fig. 12).
- The phase speeds of the breaking waves are lower than predicted by the linear dispersion relation, indicating that breaking occurs near the center of nonlinear wave groups (Fig. 13).

Because of its importance for air–sea interaction, a better understanding of wave breaking is critical for a wide variety of applications. This work shows that stereo video is a powerful tool for studying the surface geometry of breaking waves. As in the numerical simulations of Chalikov and Babanin (2012), our measurements show that whitecaps often form at crests of extreme surface slope, which are primarily formed by the nonlinear instability mechanisms of modulating wave groups. More work is needed to determine how traditional methods of measuring and describing surface waves (wave buoys, the frequency spectrum, etc.) apply to the breaking waves. In addition, the steep crests are less a predictor of future breaking than an indicator of imminent or active whitecapping. It is possible that dynamic-breaking criteria, as advocated by Song and Banner (2002) and Banner and Pierson (2007), may provide a better framework for predictive models than geometric criteria alone. Finally, it remains to be seen how whitecap geometry relates to the strength of the breaking (i.e., the whitecap dissipation), but it is likely that stereo video will be a useful tool in this problem as well. Future measurements could test, for example, the dissipation scalings of Duncan (1981) and Drazen et al. (2008).

Acknowledgments. We thank Alex de Klerk and Joe Talbert for their engineering expertise, without which this work would not have been possible. Alex Horner-Devine and Johannes Gemmrich provided valuable comments on an earlier manuscript. Thanks also to Adam Brown (APL-UW) and Jarett Goldsmith (DNV GL) for their assistance during the cruise. Many thanks to the crew of the R/V *Thomas G. Thompson*. Funding for this work was provided by the National Science Foundation (OCE-1332719). The data and processing codes used in this paper are available online (http://hdl.handle.net/1773/38314).

REFERENCES

Babanin, A., 2011: *Breaking and Dissipation of Ocean Surface Waves.* Cambridge University Press, 463 pp.

——, D. Chalikov, I. Young, and I. Savelyev, 2007: Predicting the breaking onset of surface water waves. *Geophys. Res. Lett.*, **34**, L07605, doi:10.1029/2006GL029135.

——, ——, I. R. Young, and I. Savelyev, 2010: Numerical and laboratory investigation of breaking of steep two-dimensional waves in deep water. *J. Fluid Mech.*, **644**, 433–463, doi:10.1017/S002211200999245X.

Banner, M. L., 1990: Equilibrium spectra of wind waves. *J. Phys. Oceanogr.*, **20**, 966–984, doi:10.1175/1520-0485(1990)020<0966:ESOWW>2.0.CO;2.

——, and W. L. Pierson, 2007: Wave breaking onset and strength for two-dimensional deep water wave groups. *J. Fluid Mech.*, **585**, 93–115, doi:10.1017/S0022112007006568.

——, A. V. Babanin, and I. Young, 2000: Breaking probability for dominant waves on the sea surface. *J. Phys. Oceanogr.*, **30**, 3145–3160, doi:10.1175/1520-0485(2000)030<3145:BPFDWO>2.0.CO;2.

——, X. Barthelemy, F. Fedele, M. Allis, A. Benetazzo, F. Dias, and W. L. Pierson, 2014: Linking reduced breaking crest speeds to unsteady nonlinear water wave group behavior. *Phys. Rev. Lett.*, **112**, 114502, doi:10.1103/PhysRevLett.112.114502.

Benetazzo, A., 2006: Measurements of short water waves using stereo matched image sequences. *Coastal Eng.*, **53**, 1013–1032, doi:10.1016/j.coastaleng.2006.06.012.

——, F. Fedele, G. Gallego, P.-C. Shih, and A. Yezzi, 2012: Offshore stereo measurements of gravity waves. *Coastal Eng.*, **64**, 127–138, doi:10.1016/j.coastaleng.2012.01.007.

——, F. Barbariol, F. Bergamasco, A. Torsello, S. Carniel, and M. Sclavo, 2015: Observation of extreme sea waves in a space–time ensemble. *J. Phys. Oceanogr.*, **45**, 2261–2275, doi:10.1175/JPO-D-15-0017.1.

——, ——, ——, ——, ——, and ——, 2016: Stereo wave imaging from moving vessels: Practical use and applications. *Coastal Eng.*, **109**, 114–127, doi:10.1016/j.coastaleng.2015.12.008.

Brown, M. G., and A. Jensen, 2001: Experiments on focusing unidirectional water waves. *J. Geophys. Res.*, **106**, 16 917–16 928, doi:10.1029/2000JC000584.

Chalikov, D., 2005: Statistical properties of nonlinear one-dimensional wave fields. *Nonlinear Processes Geophys.*, **12**, 671–689, doi:10.5194/npg-12-671-2005.

——, and A. V. Babanin, 2012: Simulation of wave breaking in one-dimensional spectral environment. *J. Phys. Oceanogr.*, **42**, 1745–1761, doi:10.1175/JPO-D-11-0128.1.

Cox, C., and W. Munk, 1954: Measurement of the roughness of the sea surface from photographs of the sun's glitter. *J. Opt. Soc. Amer.*, **44**, 838–850, doi:10.1364/JOSA.44.000838.

de Vries, J. J., 2014: Datawell Waverider reference manual: DWR-MkIII, DWR-G. Datawell BV Rep., 147 pp.

de Vries, S., D. F. Hill, M. A. de Schipper, and M. J. F. Stive, 2011: Remote sensing of surf zone waves using stereo imaging. *Coastal Eng.*, **58**, 239–250, doi:10.1016/j.coastaleng.2010.10.004.

Drazen, D., W. K. Melville, and L. Lenain, 2008: Inertial scaling of dissipation in unsteady breaking waves. *J. Fluid Mech.*, **611**, 307–332, doi:10.1017/S0022112008002826.

Duncan, J. H., 1981: An experimental investigation of breaking waves produced by a towed hydrofoil. *Proc. Roy. Soc. London*, **A377**, 331–348, doi:10.1098/rspa.1981.0127.

Fedele, F., A. Benetazzo, G. Gallego, P.-C. Shih, A. Yezzi, F. Barbariol, and F. Ardhuin, 2013: Space–time measurements of oceanic sea states. *Ocean Modell.*, **70**, 103–115, doi:10.1016/j.ocemod.2013.01.001.

Forristall, G. Z., 2000: Wave crest distributions: Observations and second-order theory. *J. Phys. Oceanogr.*, **30**, 1931–1943, doi:10.1175/1520-0485(2000)030<1931:WCDOAS>2.0.CO;2.

Gemmrich, J. R., and D. Farmer, 1999: Observations of the scale and occurrence of breaking surface waves. *J. Phys. Oceanogr.*, **29**, 2595–2606, doi:10.1175/1520-0485(1999)029<2595:OOTSAO>2.0.CO;2.

——, M. L. Banner, and C. Garrett, 2008: Spectrally resolved energy dissipation rate and momentum flux of breaking waves. *J. Phys. Oceanogr.*, **38**, 1296–1312, doi:10.1175/2007JPO3762.1.

Herbers, T. H. C., and T. T. Janssen, 2016: Lagrangian surface wave motion and Stokes drift fluctuations. *J. Phys. Oceanogr.*, **46**, 1009–1021, doi:10.1175/JPO-D-15-0129.1.

——, P. F. Jessen, T. T. Janssen, D. B. Colbert, and J. H. MacMahan, 2012: Observing ocean surface waves with GPS-tracked buoys. *J. Atmos. Oceanic Technol.*, **29**, 944–959, doi:10.1175/JTECH-D-11-00128.1.

Hirschmuller, H., 2008: Stereo processing by semi-global matching and mutual information. *IEEE Trans. Pattern Anal. Mach. Intell.*, **30**, 328–341, doi:10.1109/TPAMI.2007.1166.

Holthuijsen, L. H., 1983: Stereophotography of ocean waves. *Appl. Ocean Res.*, **5**, 204–209, doi:10.1016/0141-1187(83)90034-2.

——, and T. H. C. Herbers, 1986: Statistics of breaking waves observed as whitecaps in the open sea. *J. Phys. Oceanogr.*, **16**, 290–297, doi:10.1175/1520-0485(1986)016<0290:SOBWOA>2.0.CO;2.

Jähne, B., J. Klinke, and S. Waas, 1994: Imaging of short ocean wind waves: A critical theoretical review. *J. Opt. Soc. Amer.*, **11A**, 2197–2209, doi:10.1364/JOSAA.11.002197.

Kleiss, J. M., and W. K. Melville, 2011: The analysis of sea surface imagery for whitecap kinematics. *J. Atmos. Oceanic Technol.*, **28**, 219–243, doi:10.1175/2010JTECHO744.1.

Leckler, F., F. Ardhuin, C. Peureux, A. Benetazzo, F. Bergamasco, and V. Dulov, 2015: Analysis and interpretation of frequency–wavenumber spectra of young wind waves. *J. Phys. Oceanogr.*, **45**, 2484–2496, doi:10.1175/JPO-D-14-0237.1.

Liu, P. C., and A. V. Babanin, 2004: Using wavelet spectrum analysis to resolve breaking events in the wind wave time series. *Ann. Geophys.*, **22**, 3335–3345, doi:10.5194/angeo-22-3335-2004.

Liu, Y., X.-H. Yan, W. T. Liu, and P. A. Hwang, 1997: The probability density function of ocean surface slopes and its effects on radar backscatter. *J. Phys. Oceanogr.*, **27**, 782–797, doi:10.1175/1520-0485(1997)027<0782:TPDFOO>2.0.CO;2.

Longuet-Higgins, M. S., 1963: The effect of non-linearities on statistical distributions in the theory of sea waves. *J. Fluid Mech.*, **17**, 459–480, doi:10.1017/S0022112063001452.

Melville, W. K., 1996: The role of surface-wave breaking in air-sea interaction. *Annu. Rev. Fluid Mech.*, **28**, 279–321, doi:10.1146/annurev.fl.28.010196.001431.

Perlin, M., W. Choi, and Z. Tian, 2013: Breaking waves in deep and intermediate waters. *Annu. Rev. Fluid Mech.*, **45**, 115–145, doi:10.1146/annurev-fluid-011212-140721.

Phillips, O. M., 1985: Spectral and statistical properties of the equilibrium range in wind-generated gravity waves. *J. Fluid Mech.*, **156**, 505–531, doi:10.1017/S0022112085002221.

Rainey, R. C. T., and M. S. Longuet-Higgins, 2006: A close one-term approximation to the highest Stokes wave on deep water. *Ocean Eng.*, **33**, 2012–2024, doi:10.1016/j.oceaneng.2005.09.014.

Rapp, R. J., and W. K. Melville, 1990: Laboratory measurements of deep-water breaking waves. *Philos. Trans. Roy. Soc. London*, **A331**, 735–800, doi:10.1098/rsta.1990.0098.

Schwendeman, M., and J. Thomson, 2015a: A horizon-tracking method for shipboard video stabilization and rectification. *J. Atmos. Oceanic Technol.*, **32**, 164–176, doi:10.1175/JTECH-D-14-00047.1.

——, and ——, 2015b: Observations of whitecap coverage and the relation to wind stress, wave slope, and turbulent dissipation. *J. Geophys. Res. Oceans*, **120**, 8346–8363, doi:10.1002/2015JC011196.

Song, J., and M. L. Banner, 2002: On determining the onset and strength of breaking for deep water waves. Part I: Unforced irrotational wave groups. *J. Phys. Oceanogr.*, **32**, 2541–2558, doi:10.1175/1520-0485-32.9.2541.

Stansell, P., and C. MacFarlane, 2002: Experimental investigation of wave breaking criteria based on wave phase speeds. *J. Phys. Oceanogr.*, **32**, 1269–1283, doi:10.1175/1520-0485(2002)032<1269:EIOWBC>2.0.CO;2.

Stokes, G. G., 1880: On the theory of oscillatory waves. *Mathematical and Physical Papers*, Vol. 1, Cambridge University Press, 197–229, doi:10.1017/CBO9780511702242.013.

Sutherland, P., and W. K. Melville, 2013: Field measurements and scaling of ocean surface wave-breaking statistics. *Geophys. Res. Lett.*, **40**, 3074–3079, doi:10.1002/grl.50584.

Tayfun, M. A., 1986: On narrow-band representation of ocean waves: 1. Theory. *J. Geophys. Res. Oceans*, **91**, 7743–7752, doi:10.1029/JC091iC06p07743.

Thomson, J., 2012: Wave breaking dissipation observed with 'swift' drifters. *J. Atmos. Oceanic Technol.*, **29**, 1866–1882, doi:10.1175/JTECH-D-12-00018.1.

——, M. S. Schwendeman, S. F. Zippel, S. Moghimi, J. Gemmrich, and W. E. Rogers, 2016: Wave-breaking turbulence in the ocean surface layer. *J. Phys. Oceanogr.*, **46**, 1857–1870, doi:10.1175/JPO-D-15-0130.1.

Tian, Z., M. Perlin, and W. Choi, 2010: Energy dissipation in two-dimensional unsteady plunging breakers and an eddy viscosity model. *J. Fluid Mech.*, **655**, 217–257, doi:10.1017/S0022112010000832.

——, ——, and ——, 2012: An eddy viscosity model for two-dimensional breaking waves and its validation with laboratory experiments. *Phys. Fluids*, **24**, 036601, doi:10.1063/1.3687508.

Wanek, J. M., and C. H. Wu, 2006: Automated trinocular stereo imaging system for three-dimensional surface wave measurements. *Ocean Eng.*, **33**, 723–747, doi:10.1016/j.oceaneng.2005.05.006.

Weissman, M. A., S. S. Ataktürk, and K. B. Katsaros, 1984: Detection of breaking events in a wind-generated wave field. *J. Phys. Oceanogr.*, **14**, 1608–1619, doi:10.1175/1520-0485(1984)014<1608:DOBEIA>2.0.CO;2.

Williams, J. M., 1981: Limiting gravity waves in water of finite depth. *Philos. Trans. Roy. Soc. London*, **A302**, 139–188, doi:10.1098/rsta.1981.0159.

Yuen, H. C., and B. M. Lake, 1980: Instabilities of waves on deep water. *Annu. Rev. Fluid Mech.*, **12**, 303–334, doi:10.1146/annurev.fl.12.010180.001511.